Transformable *In Vivo* Robotic Laparoscopic Camera With Optimized Illumination System for Single-Port Access Surgery: Initial Prototype

Xiaolong Liu, *Member, IEEE*, Reza Yazdanpanah Abdolmalaki, *Student Member, IEEE*, Tao Zuo, Yong Guan, *Member, IEEE*, Gregory J. Mancini, and Jindong Tan, *Member, IEEE*

***Abstract*—This paper presents an initial prototype of an *in vivo* robotic laparoscopic camera that features optimized illumination to address the problems, i.e. inferior lighting uniformity and low optical efficiency, in the state-of-the-art designs of *in vivo* laparoscopic cameras. Benefiting from the transformable structure of the robotic camera, sufficient on-board space is created without sacrificing the camera's compactness to carry three dedicatedly designed freeform optical lenses for achieving the optimized illumination requirements. Designing miniature freeform optical lenses for extended light sources, such as LEDs, is a very challenging task that usually involves solving a nonstandard Monge–Ampère equation. In this paper, we approach the illumination optical design based on a ray-mapping method that is governed by a standard Monge–Ampère equation. We propose an effective numerical solver to compute the ray-mapping solution for constructing freeform lens surfaces. Experimental results prove the predicted performance of the illumination system design: greater than 97% illuminance uniformity, greater than 80% optical efficiency, and greater than 14,323 lx illuminance on a target plane with a distance of 100 mm. The effectiveness of this prototype is also experimentally verified by performing a suturing task in a simulated abdomen.**

***Index Terms*—Medical robotics, optical design, biomedical imaging.**

I. Introduction

IN MINIMALLY invasive surgery (MIS), a laparoscope has been clinically adopted for visualizing the interior of the abdominal cavity since the mid-1980s [1]. A modern laparoscope system consists of one or more high-definition (HD) digital cameras, an external light source such as xenon or light emitting diodes (LEDs) [2], a light transmission fiber-optic scope combined with other optical components for uniform illumination [3], a rod lens system for imaging, and a monitor. Superior laparoscopic imaging quality can thus be offered in terms of clarity and color definition. However, in the case of single-port access surgery, loss of triangulation between a laparoscope and other surgical instruments becomes the major disadvantage [4], which results in the clashing of instruments. In addition, counter-intuitive manipulation and limited field of view (FOV) of a laparoscope further degrade its performance in single-port access surgery. Alternatively, *in vivo* laparoscopic cameras are developed that can be fully inserted into the abdominal cavity for providing dexterous manipulation without having the abdominal wall fulcrum constraint.

For designing *in vivo* laparoscopic cameras, recent research studies have focused on developing robotic actuation mechanisms by magnetic couplings [5]–[7] and/or motor-driven articulated structures [8], [9] for pose control of the cameras, analyzing wireless transmission of imaging data and control signals via the abdominal wall [9], and clinically validating the effectiveness of *in vivo* laparoscopic cameras [10], [11]. In spite of the achieved progresses, their inferior imaging quality is a major issue that obstructs the *in vivo* camera designs to be clinically employed. It is not a straightforward task to obtain high quality images by only improving *in vivo* imaging systems with HD imaging sensors. Because for the same sensor size, the higher resolution results in the smaller pixel size that is usually with the lower light sensitivity [12]. Sufficient light intensity within a camera's FOV is a necessity to enable HD imaging sensors to work in normal condition. In addition, nonuniform lighting distribution on a target visualized area results in poor quality images with shining centers and dim margins. Furthermore, light rays that emit from the on-board light sources should be projected within a camera's FOV to maximally utilize light energy. The above requirements provide guidelines for designing an optimized illumination system in an *in vivo* laparoscopic camera.

The illumination systems that are integrated in the state-of-the-art *in vivo* laparoscopic cameras utilize bare LEDs [6], [8], [10] or LEDs stacked with reflectors [9] to realize basic illumination for the imaging sensors. To design an optimized

Manuscript received October 26, 2017; revised March 26, 2018; accepted May 19, 2018. Date of publication May 25, 2018; date of current version August 14, 2018. Recommended by Technical Editor D. Stoianovici. (*Corresponding author: Xiaolong Liu.*)

X. Liu, R. Y. Abdolmalaki, and J. Tan are with the Department of Mechanical, Aerospace and Biomedical Engineering, University of Tennessee, Knoxville, TN 37996 USA (e-mail: xliu57@vols.utk.edu; ryazdanp@vols.utk.edu; tan@utk.edu).

T. Zuo is with the College of Information Science and Engineering, Wuhan University of Science and Technology, Wuhan 430081, China (e-mail: zuotao@wust.edu.cn).

Y. Guan is with the College of Information Engineering, Capital Normal University, Beijing 100048, China (e-mail: guanyong@mail.cnu.edu.cn).

G. J. Mancini is with the Department of Surgery, University of Tennessee, Knoxville, TN 37996 USA (e-mail: GMancini@mc.utmck.edu).

Color versions of one or more of the figures in this paper are available online at http://ieeexplore.ieee.org.

Digital Object Identifier 10.1109/TMECH.2018.2840845

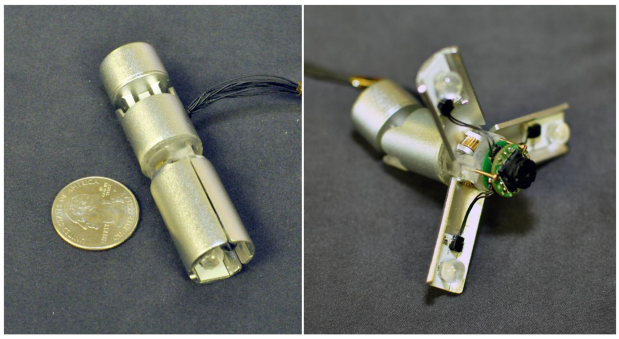

(a) (b)

Fig. 1. Prototype of the *in vivo* robotic laparoscopic camera. (a) The folded mode of the camera, which is used for inserting into a trocar. (b) The working mode of the camera.

illumination system, we need to address two major challenges: First, the robotic camera design should be compact enough to fit in the abdominal incision and meanwhile reserve sufficient on-board space to carry dedicatedly designed secondary optics[1] of LEDs. Second, to satisfy the optimized illumination requirements, freeform nonimaging optics are needed to control light beams. Designing freeform optics is a challenging task because this problem is governed by a nonstandard Monge–Ampère equation [13], [14], which is a second-order highly nonlinear partial differential equation (PDE). Moreover, the assumption of zero-étendue (point light source) will be invalid considering the comparable sizes of the LEDs and the freeform optics. This will make the design task even more difficult.

The scope of this paper is to propose a solution to develop an *in vivo* laparoscopic camera with an optimized illumination system. We intend to propel *in vivo* laparoscopic cameras to take one step towards having comparable imaging quality with the up-to-date laparoscopes. In this paper, we present an initial prototype of a transformable *in vivo* robotic laparoscopic camera, as shown in Fig. 1, which features three foldable wings for creating sufficient space to contain three high-efficiency white LEDs as the light sources and three freeform optical lenses for controlling light beams. The folded mode in Fig. 1(a) is used to insert into the abdominal cavity via an incision, while the extended mode in Fig. 1(b) is activated to expose the imaging system and the illumination system after the robotic camera being anchored against the abdominal wall. The noncoaxial arrangement of the imaging system and the illumination system introduces shadow depth cues that help surgeons to perceive three-dimensional (3-D) depth from 2-D images [15]. Freeform nonimaging optical lens design for the LEDs is one of the most critical tasks in this paper. We approach this task based on a ray-mapping method that is governed by a standard Monge–Ampère equation. We propose an effective numerical solver to compute the ray map solution for constructing freeform surfaces. To improve the degraded illumination performance that caused by extended light sources, a feedback modification scheme is introduced to adjust freeform surfaces.

[1]Secondary optics are the optics which exist outside of an LED package, such as reflectors or lenses, to create the desired illumination appearance and beam pattern.

The major contributions of this research include the following.

1) An innovative transformable robotic laparoscopic camera design, which combines compactness for fitting in the abdominal incision and sufficient on-board space for containing the optimized illumination system.
2) An effective freeform nonimaging lens design method for extended light sources, which is used for developing the optimized illumination system.
3) An experimental performance validation of an assembled illumination system with manufactured freeform lenses.
4) A surgical task demonstration by a complete initial prototype that consists of an *in vivo* robotic laparoscopic camera, an external anchoring/control unit (EACU), and a user controller for sending control signals.

II. Design of Robotic Laparoscopic Camera System

A. System Overview

The *in vivo* robotic laparoscopic camera system consists of an EACU, a robotic camera, a user controller, and a monitor, as shown in Fig. 2(a). During MIS, the robotic camera with the folded mode is inserted into the abdominal cavity via a trocar. The EACU magnetically fixes the robotic camera against the inner side of the abdominal wall. The soft cable between the EACU and the robotic camera is used for control signal transmission, imaging data acquisition, power supply, and retrieval of the robotic camera from the abdominal cavity.

A surgeon can send control signals to the microcontroller unit (MCU) in the EACU via the user controller, which controls open/close of the camera wings, pan/tilt motion to adjust the camera pose, ON/OFF of the imaging system and the illumination system, and brightness of the LEDs.

B. External Anchoring/Control Unit

The EACU is the central control unit of the whole system. Acquired surgical videos from the robotic camera is processed in the EACU and consequently send to the monitor in real time, as shown in Fig. 2(b). After receiving control commands from the user controller, the signals are processed in the MCU and transmitted to the actuator drivers, the LED driver, and the video processing unit for controlling the actuators, the LEDs, and the imaging sensor in the robotic camera.

The internal structure of the EACU is demonstrated in Fig. 3. Besides the controller circuit board, the EACU contains a diametrically magnetized external permanent magnet (EPM) that is rotationally driven by an actuator. The EPM is magnetically coupled with the robotic camera's internal permanent magnet (IPM) to provide anchoring force for the robotic camera's fixation against the abdominal wall, and spinning torque for pan motion control. The tilt motion of the robotic camera is driven by its on-board actuation mechanisms.

C. In Vivo Robotic Camera

The initial prototype of the *in vivo* robotic camera currently consists of the following three main components.

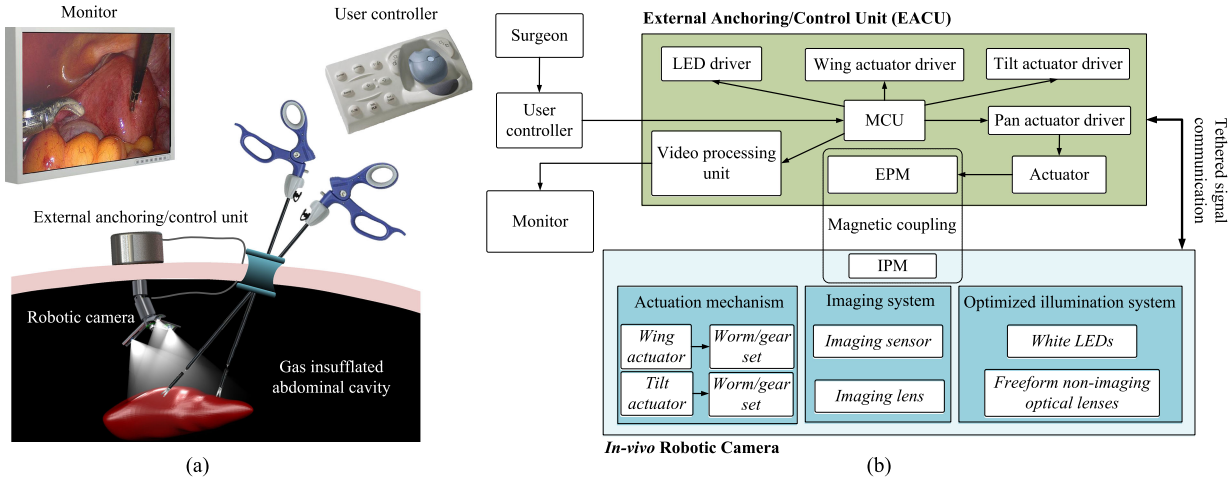

Fig. 2. Functional diagram and physical configuration of the *in vivo* robotic laparoscopic camera. (a) Conceptually demonstrates the robotic camera system working in a surgical scenario. (b) The firmware design architecture of the robotic camera system.

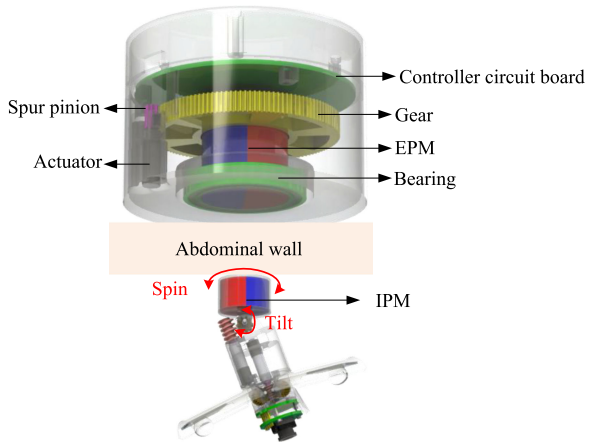

Fig. 3. Demonstration of the EACU's internal structure and the robotic camera's pose control.

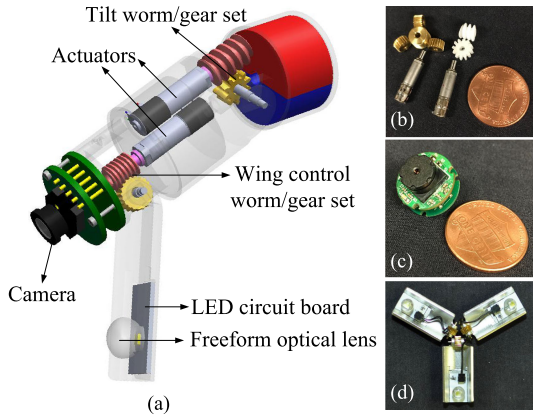

Fig. 4. Internal structure of the robotic camera. (a) Structure overview. (b) Miniature actuators and worm/gear sets. (c) Camera module integrated with an imaging lens. (d) Illumination system with LEDs and freeform optical lenses.

1) An actuation mechanism that controls the camera's tilt motion and wings' opening angle.
2) An imaging system.
3) An optimized illumination system [see Fig. 2(b)].

1) Actuation Mechanism: In addition to the pan motion actuated by the EPM, the tilt motion of the robotic camera is controlled by an on-board actuator with a set of worm and gear, as shown in Fig. 4(a). The tilt gear is fixed with the shaft and the magnet head. The actuators' housing together with the camera and the illumination system rotates around the shaft by actuating the tilt worm. The combination of pan and tilt motion enables the robotic camera to visually cover the whole surgical area. The other actuator in the housing controls the wings' opening angle by using one worm and three gears. The actuation mechanism provides a tilt motion range of 49° and wings motion range of 80° (0° for the folded mode).

Fig. 4(b) shows the components of the actuation mechanism in the prototype. The actuators are stepper motors with diameters of 4 mm, lengths of 14.42 mm, and 125:1 planetary gearheads (ZWBMD004004-125, Shenzhen Zhaowei Machinery & Electronics, Inc.). The stepper motor can deliver a torque of 10 mN·m at continuous operation. The customized worm gear sets for the tilt actuator and the wings' actuator have reduction ratios of 12:1 and 20:1, respectively.

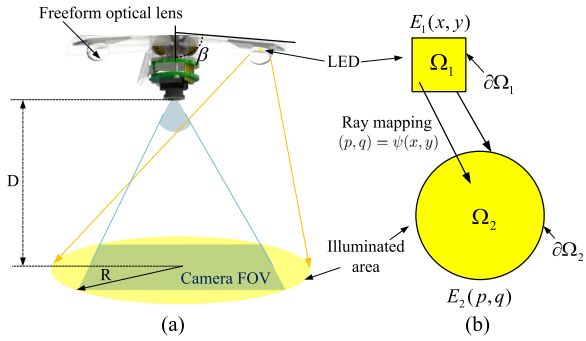

Fig. 5. (a) Configuration of optimized illumination. The camera's FOV is contained within a circular illuminated area. (b) Light energy mapping from one LED (domain Ω_1) to the circular illuminated area (domain Ω_2). $E_1(x,y)$ and $E_2(p,q)$ are illuminance distributions in Ω_1 and Ω_2 separately.

2) Imaging System: The imaging system in this initial prototype is developed to provide basic visualization functionality for evaluating the design performance of the *in vivo* robotic camera system. Fig. 4(c) shows the developed imaging system that employs the following.

1) An OmniVision OV7955 CMOS sensor with an imaging array size of 672 × 492, an optical size of 1/3.7″, a pixel size of 6 μm × 6 μm, a capture rate of 60 fps, and NTSC analog output.
2) A 1/4″ lens (DSL756, Sunex, Inc.) with a focal length of 3.8 mm, a diagonal FOV 60°, and multimegapixel resolution.
3) A compatible lens holder (CMT756, Sunex, Inc.) for the DSL756 lens.

3) Optimized Illumination System: As we discussed in Section I, the objectives of designing an optimized illumination system are sufficient light intensity, high optical efficiency, and high illuminance uniformity. In fact, defining the "sufficient light intensity" for an imaging sensor is difficult due to many factors, e.g. pixels' sensitivity, surface conditions of an illuminated area, and the aperture size of an imaging lens. But according to some experimental studies [6], a maximum illuminance of 4,000 lx at a distance of 50 mm was used to work with a similar imaging sensor as the one in our imaging system. Considering 50mm ∼ 100 mm working distance between the camera and a target area, we conservatively require our illumination system to uniformly deliver a minimum illuminance of 10,000 lx at a distance of 100 mm.

For maximizing light energy efficiency, Fig. 5(a) provides the feasible configuration that the camera's FOV fits right in the illuminated area. Due to the 60° diagonal FOV of the imaging lens, the radius of the illuminated area is calculated as $R = D \cdot \tan(60°/2)$, where D is the camera-to-target distance. When $D = 100$ mm, R should be 57.7 mm. To guarantee the area of the camera's FOV can be uniformly illuminated, R is set as 80 mm considering design tolerance.

Fig. 4(d) shows the components in the optimized illumination system. Three white LEDs (Xlamp XQ-E, Cree, Inc.) with 5700 K color temperature are employed to provide a total luminous flux of 354 lm at 350 mA. If the luminous flux of 354 lm is uniformly projected on the area with $R = 80$ mm, an average illuminance of 17,607 lx can be achieved, which is more than the required 10,000 lx. If we only use two LEDs, it seems that a total luminous flux of 236 lm can provide an average illuminance of 11,743 lx. But considering that the optical efficiency will not be 100%, using three LEDs will be able to compensate the loss of optical power. Thus, three freeform optical lenses are developed to redirect light beams for achieving the above illumination requirements. The detailed freeform optical lens design technique is proposed in the next section.

III. Freeform Optical Lens Design for Optimized Illumination System

In this section, we present an effective freeform optical lens design method for the LEDs to achieve the optimized illumination requirements. The state-of-the-art solutions to the freeform optical design problem can be categorized into two groups: directly computation; and two-step ray-mapping methods. For directly computation, this problem is governed by a nonstandard Monge–Ampère equation [13], [14], which is a second-order nonlinear PDE. Because of the highly nonlinearity of this equation, it is quite challenging to find an easy-to-implement and effective numerical method to obtain a converged solution. Instead of solving the nonstandard Monge–Ampère equation directly, two-step ray-mapping methods [16], [17] are studied to establish the relationship between emitted light rays from the light source and incident points on the target plane, and consequently to construct a freeform optical surface. The main challenge of generating a ray map is to enforce integration conditions to guarantee a smooth continuous optical surface. According to the law of conservation of energy, a ray map $(p, q) = \psi(x, y)$ [see Fig. 5(b)] is formulated in

$$\int_{\Omega_2} E_2(p,q)\,dpdq - \int_{\Omega_1} E_1(x,y)\,dxdy = 0 \tag{1}$$

where $E_1(x, y)$ and $E_2(p, q)$ are the LED illuminance distribution in the source domain Ω_1 and the prescribed target illuminance distribution in the target domain Ω_2, respectively. By representing the ray mapping solution as the gradient of a convex potential $\psi = \nabla\omega$, an equivalent form of (1) can be derived as

$$\det \nabla^2\omega(x,y) = \frac{E_1(x,y)}{E_2(\nabla\omega(x,y))}. \tag{2}$$

Numerical solvers to compute (2) are either hard to numerically implement [18], [19], or tricky to get a converged solution [20], [21]. Inspired by the fact that a weak solution of a lower order nonlinear PDE can be approximated by a sequence of higher order quasi-linear PDEs [22], we introduce an effective numerical method to compute the solution of (2) for the freeform optical lens design.

A. Ray Map Computation

We employ a sequence of fourth-order quasi-linear PDEs, i.e., the biharmonic operator [23], to approximate the numerical solution of the second-order nonlinear PDE in (2). The approximated solution ω^ϵ can be computed from the following quasi-linear PDE with a Newmann boundary condition (BC):

$$-\epsilon\Delta^2\omega^\epsilon + \det\nabla^2\omega^\epsilon - \frac{E_1(x,y)}{E_2(\nabla\omega^\epsilon(x,y))} = 0,\ (x,y) \in \Omega_1 \tag{3}$$

$$\text{BC}: \quad f(\nabla\omega^\epsilon(x,y)) = 0,\ (x,y) \in \partial\Omega_1 \tag{4}$$

where $\epsilon > 0$; f represents the mapping function from $\partial\Omega_1$ to $\partial\Omega_2$; $\partial\Omega_1$ and $\partial\Omega_2$ are the boundary regions of Ω_1 and Ω_2; If $\lim_{\epsilon\to 0^+} \omega^\epsilon$ exists, the weak solution of (3) can be found.

To compute the solution of (3), we initialize a set of ϵ in descent order. The solution of ω^ϵ at the current iteration is initialized by the solution from the previous iteration. By discretizing (3) and (4), a system of nonlinear equations is formulated as

$$\boldsymbol{S}(\boldsymbol{W}^\epsilon) = 0 \tag{5}$$

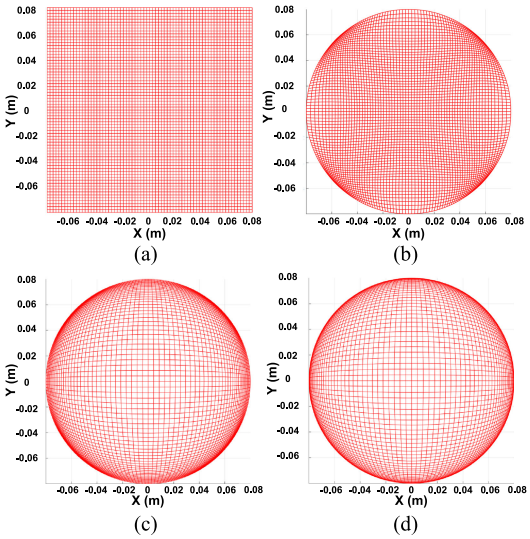

Fig. 6. Computed ray-mapping results on the target plane by using 71×71 mesh grids. (a) Initial guess of the ray map $(p, q) = \nabla\omega(x, y)$. (b) Ray-mapping result $\nabla\omega^{\epsilon}$ when $\epsilon = 1$. (c) Ray-mapping result when $\epsilon = 0.01$. (d) Ray-mapping result when $\epsilon = 0.001$.

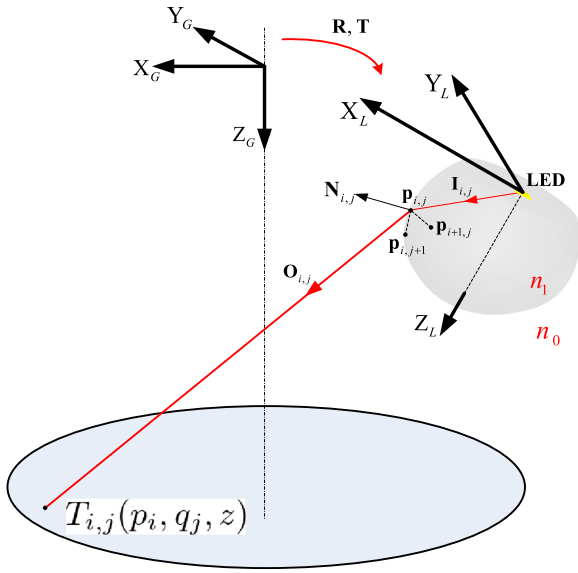

Fig. 7. Illustration of the initial optical surface construction method. **R** and **T** represent the rotational matrix and the translational vector from Σ_L to Σ_G.

where $\boldsymbol{W}^{\epsilon}$ is a vector that contains the discretized values of ω^{ϵ} in Ω_1. The Newton's method is employed to compute the solution of (5).

The illuminated area Ω_2 is set as a circular region with a radius R of 80 mm according to Section II-C3. The LEDs are initially modeled as a Lambertian point source $E_1(x, y)$. $E_2(p, q)$ is a function with a constant value in Ω_2. Optical surface modification is implemented in Section III-B2 by considering the extended light source condition.

Fig. 6 shows the computed ray maps in different iterations by using 71×71 mesh grids for discretization. To solve (5), an initial guess of $\nabla\omega$ is provided as illustrated in Fig. 6(a). It is obvious to see that when $\epsilon = 1$, all the light rays are redirected within $\partial\Omega_2$, as shown in Fig. 6(b). But the inner ray-mapping in Ω_2 is not accurate. In the following iterations, the values of ϵ are set as 0.01 and 0.001 to compute more accurate ray mapping results, as shown in Fig. 6(c) and (d). The computation is converged at the iteration of $\epsilon = 0.001$.

B. Optical Surface Construction

1) Initial Surface Construction: An initial optical surface is constructed based on the computed ray map shown in Fig. 6(d). Each light ray $\boldsymbol{I}_{i,j}$ in the coordinate system $\Sigma_L\{X_L, Y_L, Z_L\}$ corresponds to a point $T_{i,j}(p_i, q_j, z)$on the target plane $\mathbf{T}_{i,j}$ in the coordinate system $\Sigma_G\{X_G, Y_G, Z_G\}$, as shown in Fig. 7. The relationship between Σ_G and Σ_L is determined by the wings' angle β and the LED positions on the wings. We employ an easy-to-implement method proposed in [16] to construct an initial optical surface. However, due to the accumulated errors, this method cannot guarantee the computed normal vectors $\mathbf{N}_{i,j}$ at $\mathbf{p}_{i,j}$ are perpendicular to $\overrightarrow{\mathbf{p}_{i,j}\mathbf{p}_{i+1,j}}$ and $\overrightarrow{\mathbf{p}_{i,j}\mathbf{p}_{i,j+1}}$. We introduce an optimization technique to correct the normal vectors by adjusting the surface points. For each surface point, an optimization function can be constructed as

$$Q_{i,j}(\boldsymbol{\rho}) = ||(\rho_{i+1,j}\boldsymbol{I}_{i+1,j} - \rho_{i,j}\boldsymbol{I}_{i,j}) \cdot \boldsymbol{N}_{i,j}|| + ||(\rho_{i,j+1}\boldsymbol{I}_{i,j+1} - \rho_{i,j}\boldsymbol{I}_{i,j}) \cdot \boldsymbol{N}_{i,j}|| = 0$$

where $\rho_{i,j}$ represents the distance between the origin of a light source and a surface point. The nonlinear least-squares method is adopted to minimize $\sum_{i=1}^{N_i}\sum_{j=1}^{N_j} Q_{i,j}(\boldsymbol{\rho})^2$. After obtaining the optimized surface points, an optical surface can thus be constructed by using the nonuniform rational basis spline [24] method.

2) Surface Modification for Extended Light Sources: The constructed freeform optical surface is actually based on the zero-étendue assumption. In our case, we cannot neglect the size of an LED. Based on an initial desired illuminance distribution $E_2(p, q)$ on the target area, a ray map and a freeform optical lens are computed, as shown in the column of "Iteration 0" in Fig. 8(a1) and (a2). The resulted illuminance distribution by using the real size LED yields poor uniformity, as shown in Fig. 8(a3). The optical performance can be improved by employing a feedback modification scheme [25]. Modified target illuminance distribution is calculated in accordance with the simulated illuminance distributions in previous iterations

$$\widehat{E}_2^{i+1}(p, q) = \frac{E_2(x, y)}{\widetilde{E}_2^0(p, q)} \frac{E_2(p, q)}{\widetilde{E}_2^1(p, q)} \cdots \frac{E_2(p, q)}{\widetilde{E}_2^i(p, q)} E_2(p, q) \quad (6)$$

where $\widetilde{E}_2^i(p, q)$ is the simulated illuminance distribution at the ith iteration; and $\widehat{E}_2^{i+1}(x, y)$ is the modified illuminance distribution for the $(i + 1)$th iteration. For more details about our proposed freeform optical lens design method, please refer to [26].

Fig. 8 shows the modified ray maps, optical surfaces, and resulted illuminance distributions in different iterations. We sampled the results in iteration 0, 2, 4, and 6 to compare the performance differences. The ray maps and the lens profiles are

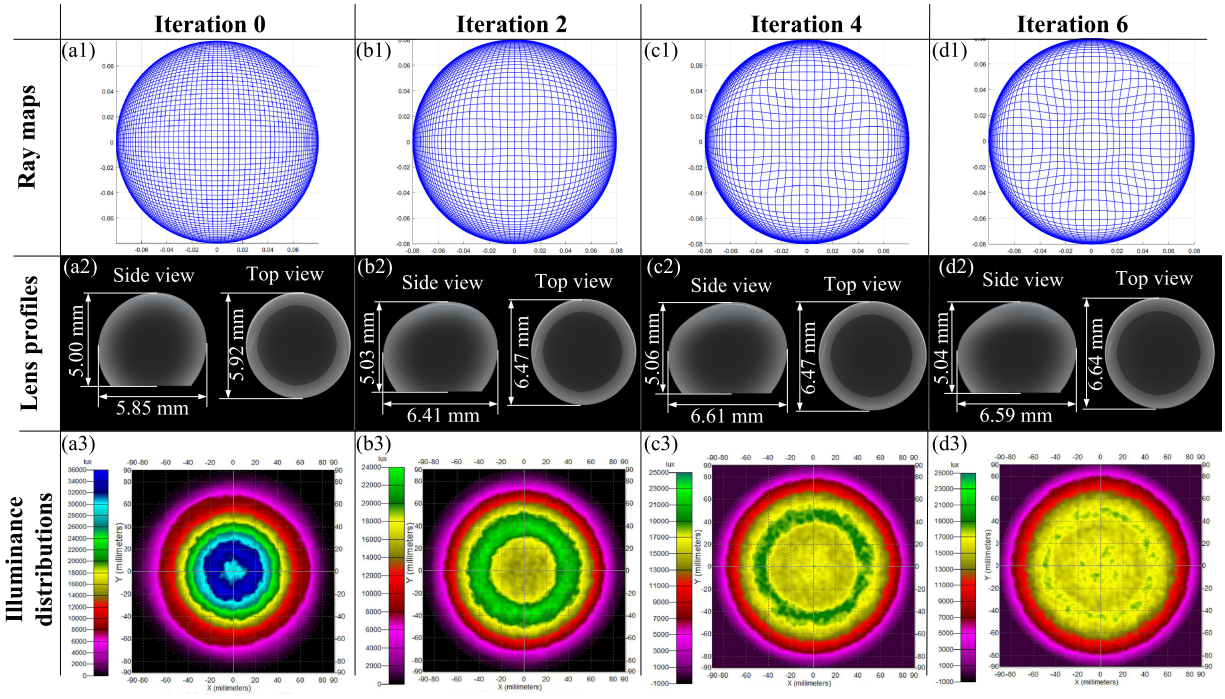

Fig. 8. Surface modification of freeform optical lenses for the LEDs.

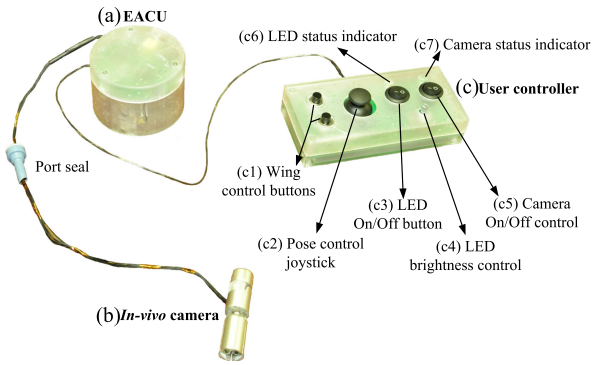

Fig. 9. Prototypes of (a) the external anchoring/driving unit, (b) the *in vivo* robotic camera, and (c) the user controller.

TABLE I
PROTOTYPE SPECIFICATIONS

	Diameter	Height	Weight
EACU	80 mm	50 mm	397.2 g
In-vivo camera	18 mm	72 mm (folded)	43.8 g
		45 mm (extended)	

adjusted based on the simulated $\widehat{E}_2^i(x, y)$ at the current iteration. It is obvious to see that the illuminance uniformity is significantly improved, as shown in Fig. 8(a3), (b3), (c3), and (d3). Recall the camera's FOV that is covered by a circular area with a radius R of 57.7 mm when $D = 100$ mm in Section II-C3. The illuminance uniformity in Fig. 8(d3) within the area with a radius R of 60 mm is 94.9%. The average illuminance in this area is 16, 132 lx. The optical efficiency is 87.49% considering the Fresnel losses.

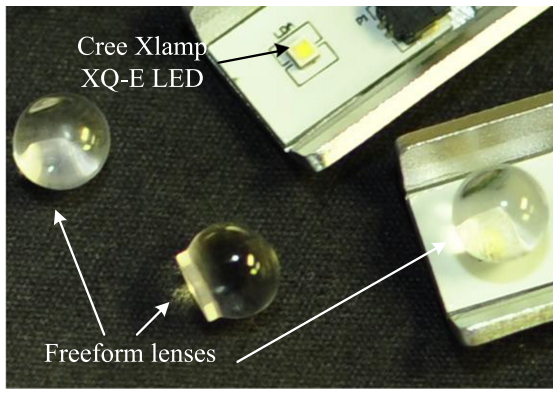

Fig. 10. Manufactured freeform optical lenses for the LEDs.

IV. EXPERIMENTS

A. Fabrication of the Robotic Camera System

Fig. 9 shows the prototype of the robotic camera system including an EACU, an *invivo* robotic camera, and a user controller. The specifications of this prototype is presented in Table I.

B. Manufacturing of Freeform Optical Lenses

The freeform lens designed in Section III was manufactured by using an ultraprecision vertical machine (UVM-450C, Toshiba, Inc.). The manufacturing accuracy is $\pm 1\,\mu$m, which is measured by using both a coordinate measurement machine and an ion beam figuring process. The material of the lenses was selected as PMMA (Polymethyl Methacrylate) with a refractive index of 1.49 and visible light transmittance of 92%.

TABLE II
SPECIFICATIONS OF THE EPM AND THE IPM

Parameters	EPM	IPM
Material	NdFeB	NdFeB
Grade	N52	N52
Magnetization Direction	Diametrically	Diametrically
Outer diameter	29 mm	16.5 mm
Inner diameter	N/A	2.5 mm
Thickness	30 mm	10 mm

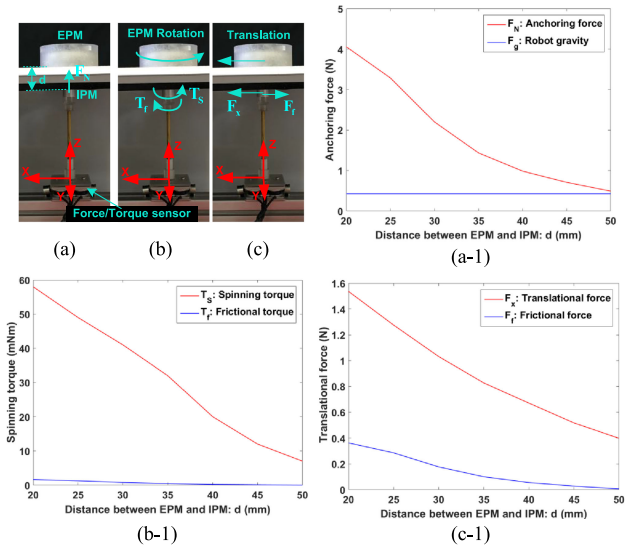

Fig. 11. Magnetic coupling tests for the EPM and the IPM. (a), (b), and (c) Experiment setups for anchoring test, spinning test, and translational test, respectively. (a)-1, (b)-1, and (c)-1 Experiment results of anchoring test, spinning test, and translational test.

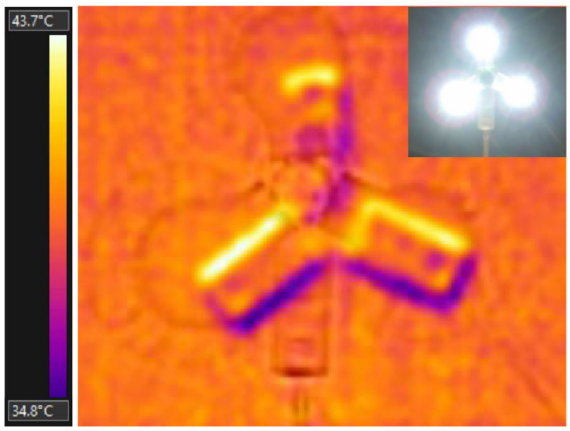

Fig. 12. Thermal image of the illumination system.

Fig. 10 shows the manufactured freeform optical lenses, Cree Xlamp XQ-E white LEDs, and LED circuit boards attached on the wings.

C. Magnetic Couping Tests Between EPM and IPM

The magnetic coupling between the EPM and the IPM provides anchoring, spinning (pan motion), and repositioning

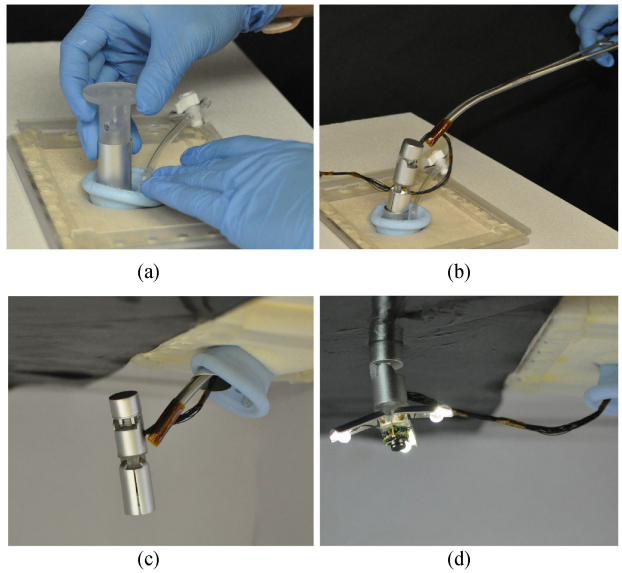

Fig. 13. Demonstration of the procedure to insert the robotic camera into a simulated abdominal cavity. (a) Applying a trocar to the SILS port. (b) Inserting the camera with forceps. (c) The camera is inserted inside the simulated abdominal cavity. (d) The camera is operated in working mode.

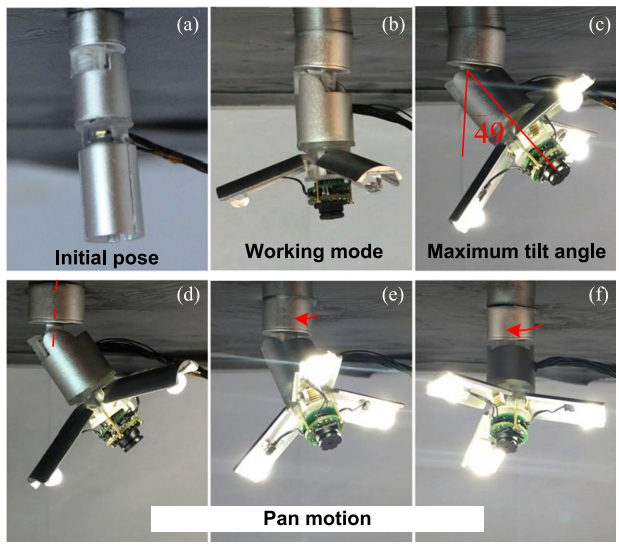

Fig. 14. Manipulation control tests of the *in vivo* robotic camera in the simulated abdominal cavity. (a) The initial pose of the robotic camera. (b) The working mode of the robotic camera. (c) The maximum tilt angle of the robotic camera. (d)–(f) The pan motion control test.

functions for the *in vivo* robotic camera. The EPM and the IPM were customized with the specifications shown in Table II. Considering that the normal range of an abdominal wall thickness is 30 mm $\sim$ 50 mm [27], we need to validate that the anchoring force F_N, spinning torque T_S, and translational force F_x can overcome the camera's gravity F_g, frictional torque T_f, and frictional force F_f, respectively, as illustrated in Fig. 11.

Fig. 11(a)–(c) shows the experimental setups by employing a six-axis force/torque sensor (HEX-58-RF-2000N, Optoforce, Inc.). The IPM was rigidly fixed with the force/torque sensor

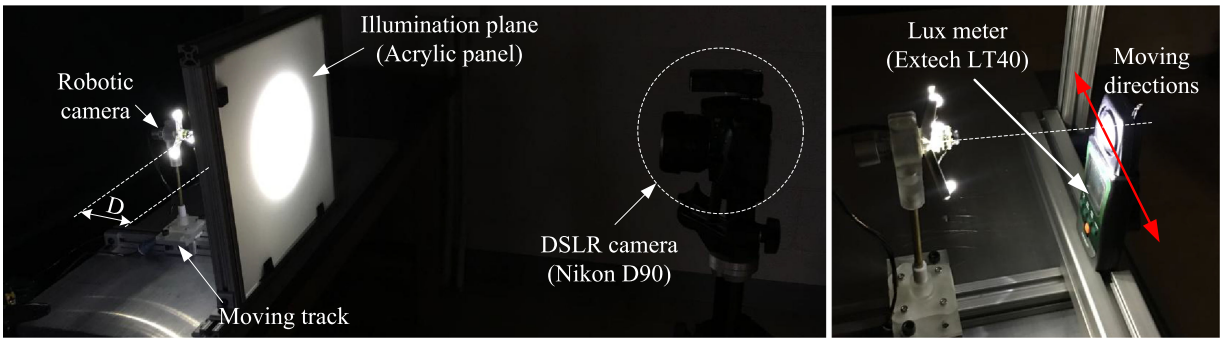

Fig. 15. Experiment setups for evaluating the performance of the optimized illumination system. (a) Experiment setup used for testing the lighting uniformity on the target plane at a distance of *D*. (b) The experiment setup for measuring illuminance values by using a lux meter.

along Z axis. In the evaluation, we set the distance d between the IPM and the EPM ranging from 20 to 50 mm with 5 mm sampling interval.

Fig. 11(a)-1 shows the comparison of measured F_N and the robotic camera's gravity $F_g = 0.43$ N. The result indicates $F_N = 4.06$ N when $d = 20$ mm, and $F_N = 0.492$ N when $d = 50$ mm, which are sufficient to compensate F_g. The maximum pressure applied on the inner abdominal wall 2.31 lbf/in^2 is less than the safe threshold 3.45 lbf/in^2 for preventing undesired histological damage [28]. Fig. 11(b)-1 shows the comparison of measured spinning torque T_S and estimated frictional torque T_f. The frictional coefficient between the IPM's case and the simulated abdominal wall is conservatively estimated as 0.1. Comparing to T_S, T_f is ignorable. Fig. 11(c)-1 shows the comparison of measured translational force F_x and the frictional force F_f. The EPM was given an offset along X direction to introduce F_x on the IPM. When $d = 20$ mm, F_x is measured as 1.53 N, while $F_f = 0.36$ N. When $d = 50$ mm, F_x is measured as 0.398 N, while $F_f = 0.012$ N.

D. Thermal Test of the Illumination System

Because of employing high-efficiency LEDs in the *in vivo* robotic camera, a thermal test of the illumination system is necessary to prevent surrounding tissue damages caused by overheating. This prototype contains a thermal management design, which utilizes aluminum PCBs for the LEDs, and three wings made by anodized aluminum as the heat sink. In the thermal test, we drove LEDs by using the maximum current 350 mA for 20 min under the room temperature 23 °C. A thermal camera (Duo^{TM} Pro R, FLIR Systems, Inc.) is used to measure the temperatures of the illumination system and its surrounding air. Fig. 12 shows the measurement result that indicates the maximum temperature 43.7 °C occurred on the wing edges. The surrounding air temperature is about 38 °C. According to [29], when tissue cells are heated to above 45 °C–50 °C, destruction of cells occurs. Therefore, the *in vivo* robotic camera can be safely manipulated in the abdominal cavity.

E. Inserting Robotic Camera Into Abdominal Cavity

Fig. 13 demonstrates the procedure to introduce the *in vivo* robotic camera into a simulated abdominal cavity via a trocar. After inserting an SILS port (Covidien port, Medtronic, Inc.) into the abdominal wall, a customized trocar, which is compatible with the 18 mm outer diameter of our *in vivo* robotic camera, can be inserted in the SILS port [see Fig. 13(a)]. Laparoscopic forceps can hold the robotic camera with folded wings to enter the abdominal cavity through the trocar [see Fig. 13(b) and (c)]. The EACU generates magnetic coupling with the IPM, and fixes the robotic camera against the inner side of the abdominal wall. The trocar is removed from the SILS port after fixing the robotic camera in the abdominal wall. Fig. 13(d) shows the working mode of the *in vivo* robotic camera by extending the wings to expose the illumination system and the imaging system in the abdominal cavity.

F. Robotic Camera Manipulation Control Tests

Fig. 14 shows manipulation control tests of the *in vivo* robotic camera in the simulated abdominal cavity. Fig. 14(a) demonstrates the initial pose of the robotic camera that is anchored against the abdominal wall. To get the robotic camera ready in the working mode, the wings are opened by pushing the wing buttons on the user controller for exposing the camera module and the illumination system in the abdominal cavity, as shown in Fig. 14(b). Fig. 14(c) demonstrates the tilt motion test of the robotic camera that achieves its maximum angle 49°. Fig. 14(d)–(f) shows pan motion test of the robotic camera, which rotates along the axis of the IPM. Combing with tilt motion and translational motion, the *in vivo* robotic camera is capable of visually covering all the surgical areas inside the abdominal cavity.

G. Performance Evaluation of Optimized Illumination System

In this part, we experimentally evaluate the performance of the optimized illumination system, which includes lighting uniformity, illuminance, and optical efficiency. Fig. 15(a) and (b) shows the experiment setups for measuring the lighting uniformity and illuminance on the target plane, respectively. In Fig. 15(a), the robotic camera was attached on a sliding track, which is used for adjusting the distance D between the camera and the target plane. We utilized an acrylic panel with 55% transparency and dimensions of 300 mm × 300 mm as the

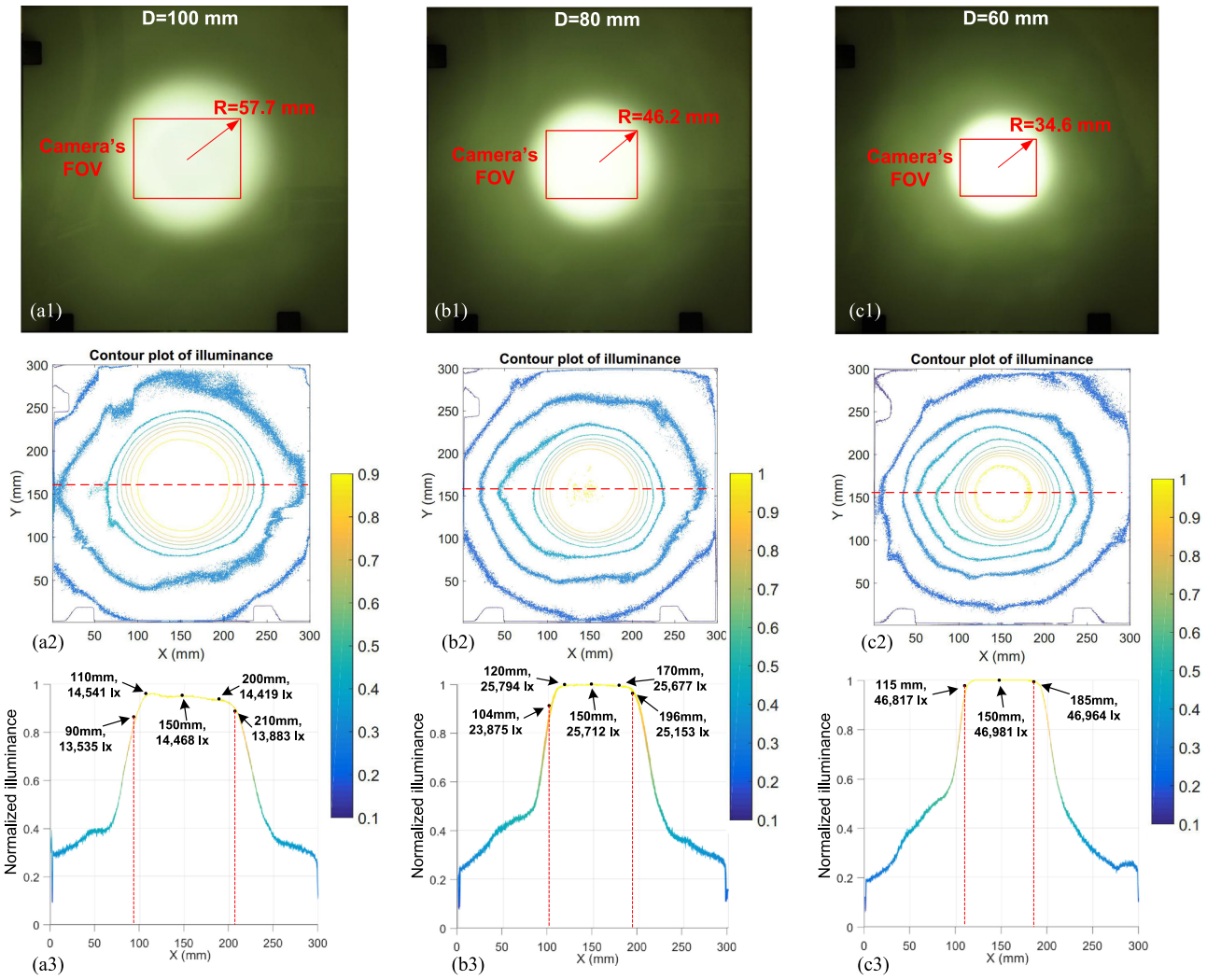

Fig. 16. Recorded experiment data and analyzed results for evaluating the performance of the optimized illumination system. (a1), (b1), and (c1) Shows the recorded illuminance distributions on the acrylic plane with the camera-to-plane distances D of 100, 80, and 60 mm. (a2), (b2), and (c2) Shows the contour plots of the normalized illuminance distributions processed from (a1), (b1), and (c1). (a3), (b3), and (c3) Demonstrates the normalized illuminance profiles of the red dash lines in (a2), (b2), and (c2), respectively. Based on the experiment setup in Fig. 15(b), the measurement locations and the measured illuminance values are indicated in (a3), (b3), and (c3).

illumination plane. A digital single-lens reflex (DSLR) camera (D90, Nikon, Inc.) was set up in front of the illumination plane, and used for recording the illuminance distribution. To measure the illuminance at a specific location, a lux meter (Extech LT-40, FLIR Systems, Inc.) was employed. The lux sensor (inside the semispherical white cover) was positioned at the height of the camera's axis, as shown in Fig. 15(b). A set of measurement points can be accessed by moving the lux meter along the red arrows.

Fig. 16(a1) shows the captured image of illuminance distribution on the target plane when $D = 100$ mm. Considering that the camera's diagonal FOV is 60°, the region of the camera's FOV on the target plane is marked by the red rectangle, which is within the illuminated area. To better visualize the illuminance uniformity, we processed the image in Fig. 16(a1) to obtain a contour plot of normalized illuminance distribution, as shown in Fig. 16(a2). We sampled the normalized illuminance data across the illumination center [the red dash line in Fig. 16(a2)], and generated a 2-D plot to show normalized illuminance versus the positions in X direction, as shown in Fig. 16(a3). The measured illuminance data as well as the measurement positions are partially indicated in Fig. 16(a3). Due to the influence of the extended light sources and the imperfect manufacturing process, the illuminance uniformity is significantly degraded when the illumination radius R is above 60 mm. We have predicted this situation at the beginning of our design. That is why we

TABLE III
PERFORMANCE OF THE OPTIMIZED ILLUMINATION SYSTEM

	D=100 mm	D=80 mm	D=60 mm
Uniformity	98.17%	97.68%	98.31%
Avg. illuminance	14,323 lx	25,408 lx	46,897 lx
Optical efficiency	80.14%	84.76%	85.92%

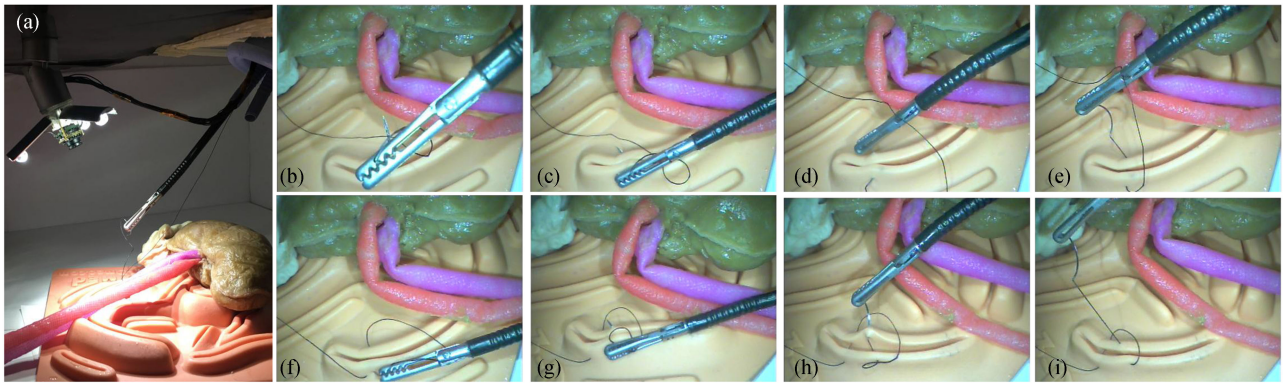

Fig. 17. Performance evaluation of the robotic camera by implementing a suturing task in the simulated abdominal cavity. (a) The instruments setup of the surgical task. (b)–(i) The sampled images recorded by the robotic camera.

initialized the illumination area with a radius of $R = 80$ mm. Similar interpretations apply to Fig. 16(b1)–(b3) with $D = 80$ mm and Fig. 16(c1)–(c3) with $D = 60$ mm.

The quantification of illuminance uniformities employs the experiment data in Fig. 16(a3) with $x = 90$ mm $\sim$ 210 mm, Fig. 16(b3) with $x = 104$ mm $\sim$ 196 mm, and Fig. 16(c3) with $x = 115$ mm $\sim$ 185 mm. For each case, the illuminance uniformity U can be computed by

$$U = (1 - \sigma/\mu) \times 100\% \tag{7}$$

where σ and μ are the standard deviation and the mean value of the sampled illuminance data. To estimate the optical efficiency of the illumination system, we compute the luminous flux projected on the illuminated areas by using

$$\Phi = \int_0^{2\pi} \int_0^{R_i} E_2'(r) \cdot r dr d\theta \tag{8}$$

where $E_2'(r)$ represents an illuminance function modeled by the sampled illuminance data shown in Fig. 16(a3), (b3), and (c3). We shifted the y axes to x = 150 mm for $E_2'(r)$. r denotes the x coordinate in the new coordinate frame. We set R_i as 80 mm, 64 mm, and 48 mm for the cases in Fig. 16(a3), (b3), and (c3), respectively. The total emitting luminous flux is 354 lm. An optical efficiency can thus be calculated by $\Phi/354$. In consequence, the performance of the optimized illumination system is quantified in Table III. The illumination system yields illuminance uniformities above 97% within the area of the camera's FOV in all the three cases, which are slightly higher than the simulated result in Section III-B2. This situation is caused by limited traced rays (0.5 million) in the optical design software. The average illuminance can reach 14,323 lx when $D = 100$ mm, which fulfills the design requirement of a minimum 10,000 lx. While the camera to target distance gets closer, the average illuminance significantly increases. The light brightness control button on the user controller can thus be adjusted for avoiding overexposure. The optical efficiencies are computed as 80.14%, 84.76%, and 85.92%, respectively. These values are slightly lower than the predicted 87.49% in Section III-B2. It is most likely because of the manufacturing flaws of the lenses on LED's contacting surface. The optical efficiency is likely to get improved by using injection molding method for future lens manufacturing.

H. Suturing Task in Simulated Abdominal Cavity

Fig. 17 demonstrates the performance evaluation of our *in vivo* robotic laparoscopic camera for single-port laparoscpic surgery. We carried out a suturing task in the simulated abdominal cavity, which was completely sealed (no extra light sources besides the illumination system). Fig. 17(a) shows that the laparoscopic forceps, which handled a curved sewing needle, were guided by the robotic camera to complete the suturing task. Fig. 17(b)–(i) shows sampled video frames recorded from the robotic camera during the surgical task. As shown in Fig. 17(b)–(i), the light rays are uniformly distributed in the camera's FOV with sufficient intensity. This evaluation provides an initial evidence to demonstrate the effectiveness of our *in vivo* robotic laparoscopic camera.

V. Conclusion

In this paper, we present an initial prototype of a transformable *in vivo* robotic camera system integrated with an optimized illumination system for single-port laparoscopic surgery. This prototype includes an EACU, an *in vivo* robotic camera, and a user controller. The key innovation of this paper is to introduce freeform optical lenses into the *in vivo* robotic camera for controlling light beams from the LEDs to achieve optimized illumination. To design freeform lenses, we propose an effective ray-mapping-based numerical computation method for the freeform optical lens design. The resulted illumination system features greater than 97% illuminance uniformity, greater than 80% optical efficiency, and greater than 14,323 lx illuminance on the target area when the camera-to-target distance ranges from 50 to 100 mm. In the experiment, we demonstrate controllability of the robotic camera, performance of the optimized illumination system, and effectiveness to apply the robotic camera in a suturing task by using a simulated abdominal cavity.

Further improvements based on this prototype will include waterproof design of the *in vivo* electronic system, reducing tethered wires for more flexible manipulation, sterilization

compatible design, etc. Considering the limitation of the compatible abdominal wall thickness range (i.e., 20 mm $\sim$ 50 mm) in this initial prototype, a series of EPM models in the EACU will be developed to cover the wide range of patients' abdominal wall thicknesses.

As what we discussed in Section I, the ultimate goal of this research is to develop a high-performance *in vivo* robotic camera with superior imaging quality to compete with state-of-the-art "long-stick" laparoscopes. The achieved optimized illumination is only one step towards this goal. We are currently developing an optimized imaging system combined with the developed illumination system to achieve superior laparoscopic imaging quality.

REFERENCES

[1] S. Spaner and G. Warnock, "A brief history of endoscopy, laparoscopy, and laparoscopic surgery," *J. Laparoendosc. Adv. Surg. Tech. A*, vol. 7, no. 6, pp. 369–373, 1997.

[2] N. Clancy, J. Clark, D. Noonan, G. Yang, and D. Elson, "Light sources for single-access surgery," *Surg. Innov.*, vol. 19, no. 2, pp. 134–44, 2012.

[3] R. Wu, Y. Qin, and H. Hua, "Improved illumination system of laparoscopes using an aspherical lens array," *Biomed. Opt. Exp.*, vol. 7, no. 6, pp. 2237–2248, Jun. 2016.

[4] P. P. Rao, P. P. Rao, and S. B. S, "Single-incision laparoscopic surgery - Current status and controversies," *J. Minimal Access Surg.*, vol. 7, no. 1, pp. 6–16, 2011.

[5] X. Liu, G. J. Mancini, and J. Tan, "Design of a unified active locomotion mechanism for a capsule-shaped laparoscopic camera system," in *Proc. IEEE Int. Conf. Robot. Autom.*, 2014, pp. 2449–2456.

[6] M. Simi *et al.*, "Magnetically activated stereoscopic vision system for laparoendoscopic single-site surgery," *IEEE/ASME Trans. Mechatronics*, vol. 18, no. 3, pp. 1140–1151, Jun. 2013.

[7] X. Liu, G. J. Mancini, Y. Guan, and J. Tan, "Design of a magnetic actuated fully insertable robotic camera system for single-incision laparoscopic surgery," *IEEE/ASME Trans. Mechatronics*, vol. 21, no. 4, pp. 1966–1976, Aug. 2016.

[8] T. Hu, P. K. Allen, N. J. Hogle, and D. L. Fowler, "Insertable surgical imaging device with pan, tilt, zoom, and lighting," *Int. J. Robot. Res.*, vol. 28, no. 10, pp. 1373–1386, 2009.

[9] C. A. Castro *et al.*, "A wireless robot for networked laparoscopy," *IEEE Trans. Biomed. Eng.*, vol. 60, no. 4, pp. 930–936, Apr. 2013.

[10] J. Cadeddu *et al.*, "Novel magnetically guided intra-abdominal camera to facilitate laparoendoscopic single-site surgery: Initial human experience." *Surg. Endosc.*, vol. 23, no. 8, pp. 1894–1899, 2009.

[11] P. Swain, R. Austin, K. Bally, and R. Trusty, "Development and testing of a tethered, independent camera for notes and single-site laparoscopic procedures," *Surg. Endosc.*, vol. 24, no. 8, pp. 2013–21, 2010.

[12] J. Farrell, F. Xiao, and S. Kavusi, "Resolution and light sensitivity tradeoff with pixel size," in *Proc. SPIE Electron. Imaging Conf.*, 2006, vol. 6069, pp. 211–218.

[13] J. S. Schruben, "Formulation of a reflector-design problem for a lighting fixture," *J. Opt. Soc. Amer.*, vol. 62, no. 12, pp. 1498–1501, 1972.

[14] H. Ries and J. Muschaweck, "Tailored freeform optical surfaces," *J. Opt. Soc. Amer. A*, vol. 19, no. 3, pp. 590–595, 2002.

[15] G. B. Hanna, A. B. Cresswell, and A. Cuschieri, "Shadow depth cues and endoscopic task performance," *Arch. Surg.*, vol. 137, no. 10, pp. 1166–1169, 2002.

[16] L. Wang, K. Qian, and Y. Luo, "Discontinuous free-form lens design for prescribed irradiance," *Appl. Opt.*, vol. 46, no. 18, pp. 3716–3723, 2007.

[17] F. R. Fournier, W. J. Cassarly, and J. P. Rolland, "Fast freeform reflector generation using source-target maps," *Opt. Express*, vol. 18, no. 5, pp. 5295–5304, 2010.

[18] K. Brix, Y. Hafizogullari, and A. Platen, "Designing illumination lenses and mirrors by the numerical solution of Monge-Ampère equations," *J. Opt. Soc. Amer. A*, vol. 32, no. 11, pp. 2227–2236, 2015.

[19] B. D. Froese, "A numerical method for the elliptic Monge-Ampère equation with transport boundary conditions," *SIAM J. Sci. Comput.*, vol. 34, no. 3, pp. A1432–A1459, 2012.

[20] M. M. Sulman, J. Williams, and R. D. Russell, "An efficient approach for the numerical solution of the Monge-Ampère equation," *Appl. Numer. Math.*, vol. 61, no. 3, pp. 298–307, 2011.

[21] R. Wu *et al.*, "Freeform illumination design: A nonlinear boundary problem for the elliptic Monge-Ampére equation," *Opt. Lett.*, vol. 38, no. 2, pp. 229–231, 2013.

[22] M. G. Crandall and P. L. Lions, "Viscosity solutions of Hamilton-Jacobi equations," *Trans. Amer. Math. Soc.*, vol. 277, no. 1, pp. 1–42, 1983.

[23] X. Feng and M. Neilan, "Vanishing moment method and moment solutions for fully nonlinear second order partial differential equations," *J. Sci. Comput.*, vol. 38, no. 1, pp. 74–98, 2009.

[24] L. Piegl and W. Tiller, *The NURBS Book*, 2nd ed. New York, NY, USA: Springer, 1997.

[25] Y. Luo, Z. Feng, Y. Han, and H. Li, "Design of compact and smooth free-form optical system with uniform illuminance for led source," *Opt. Express*, vol. 18, no. 9, pp. 9055–9063, Apr. 2010.

[26] X. Liu, R. A. Yazdanpanah, G. J. Mancini, and J. Tan, "Optical design of an *in vivo* laparoscopic lighting system," *J. Biomed. Opt.*, vol. 22, 2017, Art. no. 125003.

[27] C. Song, A. Alijani, T. Frank, G. Hanna, and A. Cuschieri, "Mechanical properties of the human abdominal wall measured in vivo during insufflation for laparoscopic surgery," *Surg. Endosc. Interventional Techn.*, vol. 20, no. 6, pp. 987–990, 2006.

[28] S. Best *et al.*, "Magnetic anchoring and guidance system instrumentation for laparo-endoscopic single-site surgery/natural orifice transluminal endoscopic surgery: Lack of histologic damage after prolonged magnetic coupling across the abdominal wall," *Urology*, vol. 77, no. 1, pp. 243–247, 2011.

[29] S. Tungjitkusolmun *et al.*, "Three-dimensional finite-element analyses for radio-frequency hepatic tumor ablation," *IEEE Trans. Biomed. Eng.*, vol. 49, no. 1, pp. 3–9, Jan. 2002.

Xiaolong Liu (M'12) received the Ph.D. degree in biomedical engineering from the University of Tennessee, Knoxville, TN, USA, in 2015.

He is currently a Research Assistant Professor with the University of Tennessee. His research interests include surgical robotics, biomedical optics, medical devices, and magnetic actuation.

Reza Yazdanpanah Abdolmalaki (S'15) received the B.S. degree in mechanical engineering from Amirkabir University of Technology, Tehran, Iran, in 2011, and the M.S. degree from University of Tehran, Tehran, Iran, in 2014, respectively. He is currently working toward the Ph.D. degree with the department of Mechanical, Biomedical and Aerospace Engineering, University of Tennessee, Knoxville, TN, USA.

His current research interests include surgical robotics, control systems, robotics, and engineering design.

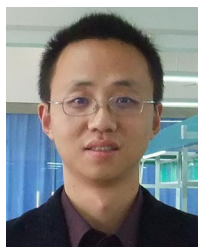

Tao Zuo received the B.S degree in communicaion engineering from Huazhong University of Science and Technology, Wuhan, China, in 1999, and the M.S and Ph.D. degrees in communication engineering from Wuhan University, Wuhan, China, in 2005 and 2011, respectively.

He is currently an Associate Professor with the College of Information Science and Engineering, Wuhan University of Science and Technology, Wuhan, China. His research interests include target tracking and intelligent robotics.

Yong Guan (M'01) received the Ph.D. degree in computer science from China University of Mining and Technology, Beijing, China, in 2004.

He is currently a Professor with Capital Normal University, Beijing, China. His research interests include formal verification, PHM for power, and embedded system design.

Dr. Guan is a member of the Chinese Institute of Electronics Embedded Expert Committee.

Gregory J. Mancini received the M.D. degree in general surgery from the Mercer University School of Medicine, Macon, GA, USA, in 2000.

He is currently an Associate Professor of Surgery with the University of Tennessee, Knoxville, TN, USA. His clinical practice and academic efforts focus on the area of minimally invasive surgery. He presents and teaches extensively both regionally and internationally on the topics of acid reflux, hernia, and bariatric surgery.

Dr. Mancini is board certified in General Surgery by the American Board of Surgery and is a Fellow of the American College of Surgeons.

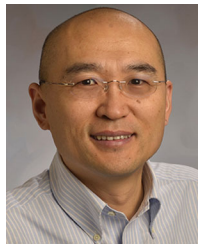

Jindong Tan (M'02) received the Ph.D. degree in electrical and computer engineering from Michigan State University, East Lansing, MI, USA, in 2002.

He is currently a Professor and an Associate Department Head with the Department of Mechanical, Aerospace and Biomedical Engineering, University of Tennessee, Knoxville, TN, USA. He has been an Assistant/Associate Professor with the Department of Electrical and Computer Engineering, Michigan Technological University, Houghton, MI, USA. His current research interests include mobile sensor networks, augmented reality and biomedical imaging, dietary assessment, and mobile manipulation.